

A Subspace Projection Approach For Wall Clutter Mitigation in Through-the-Wall Radar Imaging

Fok Hing Chi Tive, *Member, IEEE*, Abdesselam Bouzerdoun, *Senior Member, IEEE*
and Moeness G. Amin, *Fellow, IEEE*

Abstract

One of the main challenges in through-the-wall radar imaging is the strong front wall returns, which tend to obscure indoor stationary targets, rendering target detection and classification difficult, if not impossible. In this paper, we propose an effective wall clutter mitigation approach for TWRI that does not require knowledge of the background scene, nor does it rely on accurate modeling and estimation of wall parameters. The proposed approach is based on the relative strength of the front wall returns compared to behind-wall targets. It applies an eigendecomposition method to the data matrix constructed from the frequency-space measurements to identify the wall subspace. Orthogonal subspace projection is performed to remove the wall electromagnetic signature from the radar signals. The paper provides an analysis of the wall and target subspace characteristics, demonstrating that both the wall and target subspaces can be multi-dimensional. While the wall subspace depends on the wall-type and building material, the target subspace depends on its spatial extent and location, as well as the number of targets in the scene. Experimental results using synthetic and real data demonstrate the effectiveness of the subspace projection method in mitigating wall clutter while preserving the target image. It is shown that the performance of the proposed approach, in terms of the improvement factor of the target-to-wall-clutter ratio, is better than existing approaches and is comparable to that of background subtraction, which requires knowledge of a reference background scene.

Index Terms

Through-the-wall radar imaging, singular value decomposition, wall subspace, target subspace, subspace projection.

F. H. C. Tive and A. Bouzerdoun are with the School of Electrical, Computer and Telecommunications Engineering, University of Wollongong, Northfields Avenue, Wollongong NSW 2522, Australia (e-mail: {tive, a.bouzerdoun}@uow.edu.au). This work is supported by a grant from the Australian Research Council (ARC)

M. G. Amin is with the Radar Imaging Lab, Center for Advanced Communications, Villanova University, PA 19085 USA (e-mail: moeness.amin@villanova.edu). This work of Dr. Amin is supported by ONR, grant N00014-11-0576.

I. INTRODUCTION

Through-the-Wall Radar Imaging (TWRI) is an emerging technology of increasing interest. The main objective is to sense through the wall and inside enclosed building structures by using electromagnetic (EM) waves for determining the building layouts, discerning the intent of activities inside the building, and detecting, identifying and tracking moving targets. This type of technology is highly desirable in search-and-rescue missions, behind-wall target detection, and surveillance and reconnaissance in urban environments [1]–[4]. One of the main issues of imaging stationary targets is the large clutter induced by the front wall, which is usually a highly reflective and attenuative medium.

Most TWRI studies dealing with stationary targets [5]–[7] assume to have access of a background or reference scene, where background subtraction is performed on the raw data prior to applying delay-and-sum beamforming (DS) for image formation. This approach, though effective in removing wall returns, is not feasible in practice. Different approaches have been proposed to deal with strong wall reflections without relying on the background scene data [8]–[10], [13]. From the received signals, especially the first wave arrivals, it is possible to estimate the front wall parameters, such as dielectric constant and thickness [10]. The estimated parameters can be used to model the electromagnetic (EM) wall returns, which are subsequently subtracted from the total radar returns, rendering the received signal free of the wall EM signature. This approach requires accuracy in parameter estimation and modeling. Another method of suppressing the wall reflections is to use three antenna arrays placed parallel to the wall at different heights, where the upper and lower arrays comprise receivers and the middle array consists of transmitters [9]. A simple subtraction of the radar returns from the lower and upper arrays can lead to wall clutter reduction. Due to the receiver symmetry with respect to the transmitter, the contribution of the reflection from the wall in the difference signal is suppressed. In this scheme, two additional arrays are required and the effect of the subtraction operation on the target reflections is unknown and cannot be controlled. In [8], the authors proposed a spatial filtering method for wall clutter mitigation. This method relies on invariance of the wall characteristic and is based on the assumption that the wall returns have the same characteristics with changing antenna location. This spatial invariance can be horizontal, vertical, or along both dimensions in the wall plane. In this case, the application of a notch filter across the array aperture can remove the zero-frequency or low spatial frequencies, which capture constant or slowly varying wall returns. It is noted, however, that the filtering based approach is effective only for homogeneous or near-homogeneous walls and at low operating frequencies.

In this paper, we assume that the scene is stationary, and hence change detection or Doppler processing is not applicable for wall clutter removal. We present a new subspace method for mitigating wall clutter, or at least significantly suppressing it, to reveal the targets behind the wall. The proposed technique first identifies the wall clutter and target signal subspaces using singular value decomposition (SVD); then, it projects the radar signal onto a subspace orthogonal to the wall subspace. SVD has been used previously in GPR (ground-penetrating radar) to improve the signal-to-noise ratio (SNR) of the radar images [11], [12]; the B-scan image is decomposed into several eigen-images and the first eigen-image is considered the target image. In [13]–[15], the authors proposed an

SVD-based method to remove the wall clutter and to detect behind-the-wall targets from B-scan images. There, it is assumed that the wall clutter resides in the first eigen-image, whereas the target reflections reside in second eigen-image. More recently, Riaz and Ghafoor extended the SVD-based wall clutter mitigation method to multidimensional target subspace, always assuming that the wall clutter is captured by the first eigen-image [16]. However, in [17] and [18], we have shown that the wall clutter is generally characterized by a high dimensional subspace. Furthermore, the weak wall singular components may be interleaved with the target singular components. Therefore, a more effective technique is required to segregate the wall and target subspaces since the first singular component is unlikely to account for all wall clutter signal.

This paper extends our previous work [17], [18] in both analysis and experimentation. It considers SVD of the data matrix constructed from stepped-frequency matched filtered measurements obtained at different antenna positions. In so doing, it operates on the data and not on the beamformed image. The results of the two operations are entirely different due to the target localization through coherent combining. We show that, in near field imaging, the wall returns can span a multi-dimensional subspace, which depends, among other factors, on the periodic structure of the wall, the frequency response, the uniformity of the wall thickness, and the array geometry. Moreover, the target reflections can span a subspace whose dimension depends on the spatial extent of the target, the target location, the number of targets, and the configuration of the antenna array. Both empirical data and simulation confirm that the wall returns generally span a multi-dimensional subspace, where the significant target singular components can be interleaved with the wall singular components. The paper conducts a comprehensive analysis of the wall and target eigen-subspaces. Furthermore, it presents a subspace classification method to segregate between the target and wall subspaces. A subspace project method is then proposed for wall clutter mitigation, which works on the frequency-space data matrix instead of the formed image.

The remainder of the paper is organized as follows. The next section presents the geometric model of TWRI and describes delay-and-sum beamforming for image formation. Section III presents the analysis of the wall and target eigen-structures supported by simulation results. Section IV describes the proposed subspace projection approach for wall clutter mitigation. Experimental results using real data are given in Section V. Finally, the conclusion is presented in Section VI.

II. THROUGH WALL RADAR IMAGING MODEL

There are several imaging formation approaches for TWRI including tomographic approaches, differential synthetic aperture radar (SAR), compressed sensing, and adaptive beamformers. Here, we use delay-and-sum beamforming for image reconstruction. Furthermore, we apply the geometric model of TWRI as described in [19] to estimate the signal propagation delay in the presence of a wall. For completeness, we briefly review the TWRI geometry that will be used for the explanation of the proposed wall clutter mitigation approach. For simplicity, the imaging scheme is firstly derived for free-space and then extended to imaging behind a homogeneous wall. The case of heterogeneous walls will be treated in the experimental section when consider real data.

In a free-space, the geometric model is depicted in Fig. 1(a). The ground-based SAR radar system has an N -element array for two-dimensional (2-D) imaging. A local coordinate system is defined to represent the region of interest with the horizontal and vertical axes denoted as z' and x' , respectively. The center of the scene is at $(0, 0)$ and θ_n is the viewing angle of the n -th antenna. Let $R_n(0, 0)$ and c_n denote the distances from the n -th antenna to the center of the scene and to the center of the array aperture, respectively. The distance from the n -th antenna to the pixel location (z'_p, x'_p) within the region of interest is denoted as $R_n(z'_p, x'_p)$ and can be approximated by [19]

$$R_n(z'_p, x'_p) \approx R_n(0, 0) + z'_p \cos(\theta_n) - x'_p \sin(\theta_n). \quad (1)$$

The viewing angle θ_n of the n -th antenna is given by

$$\theta_n = \sin^{-1} \left(\frac{c_n}{R_n(0, 0)} \right). \quad (2)$$

Without loss of generality, let us assume a single target located at (z'_p, x'_p) . The two-way propagation delay $\tau_n(z'_p, x'_p)$ from the n -th antenna to the target is given by

$$\tau_n(z'_p, x'_p) = \frac{2}{c} (R_n(0, 0) + z'_p \cos(\theta_n) - x'_p \sin(\theta_n)). \quad (3)$$

In the presence of a homogeneous wall, the two-way propagation delay of the radar signal from the n -th antenna to the target can be rewritten as

$$\tilde{\tau}_n(z'_p, x'_p) = \frac{2}{c} (R_{n,air1}(z'_p, x'_p) + \sqrt{\epsilon} R_{n,w}(z'_p, x'_p) + R_{n,air2}(z'_p, x'_p)), \quad (4)$$

where ϵ is the relative permittivity of the wall and $R_{n,air1}(z'_p, x'_p)$, $R_{n,w}(z'_p, x'_p)$, and $R_{n,air2}(z'_p, x'_p)$ denote, respectively, the distances traveled by the signal from the n -th antenna to the target at location (z'_p, x'_p) before, through, and after the wall. These distances can be estimated as follows [7]:

$$R_{n,air1}(z'_p, x'_p) = \frac{z_o}{\cos(\varphi_n(z'_p, x'_p))}, \quad (5)$$

$$R_{n,w}(z'_p, x'_p) = \frac{d}{\cos(\phi_n(z'_p, x'_p))}, \quad (6)$$

$$R_{n,air2}(z'_p, x'_p) = \frac{z_t}{\cos(\varphi_n(z'_p, x'_p))}, \quad (7)$$

where d is the wall thickness, z_t is the distance from the wall to the target, z_o is the standoff distance from the radar to the wall, and $\varphi_n(z'_p, x'_p)$ and $\phi_n(z'_p, x'_p)$ are the angles of incidence and refraction from the n -th antenna to the pixel at location (z'_p, x'_p) , respectively, see Fig. 1(b).

Suppose that a stepped-frequency radar is used to interrogate the scene by emitting monochromatic signals with frequencies equispaced over the desired bandwidth $\omega_{M-1} - \omega_0$:

$$\omega_m = \omega_0 + m\Delta\omega, \quad \text{for } m = 0, \dots, M-1, \quad (8)$$

where ω_0 is the lowest frequency in the desired frequency band, $\Delta\omega$ is the frequency step size, and M is the total number of frequencies. With DS beamforming, the complex amplitude of the pixel at location (z, x) is given by

$$I(z, x) = \frac{1}{NM} \sum_{n=0}^{N-1} \sum_{m=0}^{M-1} s(m, n) \exp(j\omega_m \tilde{\tau}_n(z, x)), \quad (9)$$

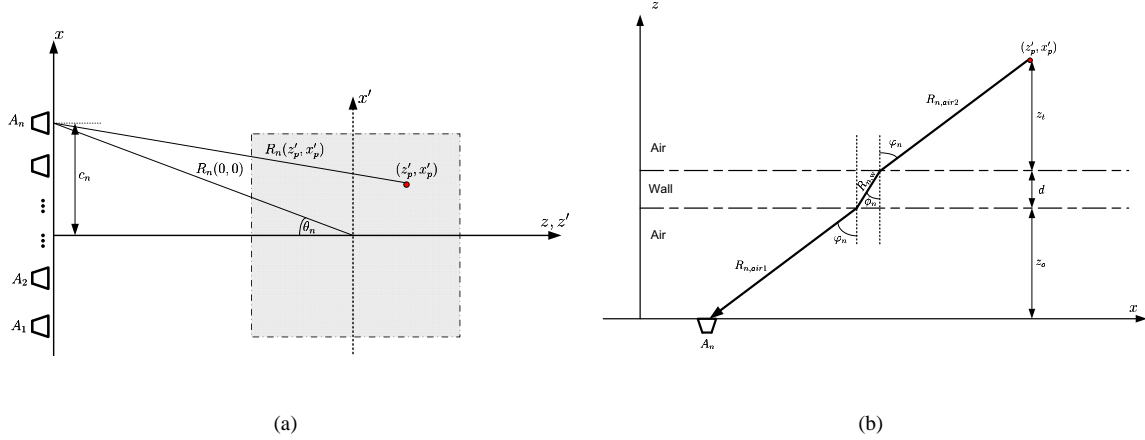


Fig. 1. Through-the-wall radar imaging geometry: (a) in frees-space and (b) through the wall.

where $s(m, n)$ is the radar signal of m -th frequency received at the n -th antenna and $\tilde{\tau}_n(z, x)$ denotes the focusing delay for the pixel at location (z, x) with respect to the n -th antenna, including the propagation through the wall. In the succeeding section, we present the analysis of the wall and target eigen-subspaces.

III. EIGEN-SUBSPACE ANALYSIS OF WALL AND TARGET

Many existing SVD-based wall clutter mitigation approaches assume that the wall reflections are characterized by the first singular vector associated with the most dominant singular value [13]–[16]. In [17], [18], we have shown that multiple singular vectors can span the wall subspace. In this section, we investigate the factors affecting the wall and target eigen-subspaces. The dimension of the wall subspace is related to, among other factors, the wall heterogeneity, the wall thickness uniformity, and the antenna array configuration. For the target subspace, its dimension is affected by the target location, the spatial extent of the target, the number of targets behind the wall, and the configuration of the array aperture. Results from simulations and real experiments are included to support the analysis of the wall and target subspaces.

A. Wall Eigen-Subspace

In practical TWRI applications, we often deal with two types of walls: homogeneous and heterogeneous walls. For homogeneous walls, the wall characteristics are spatially shift-invariant along both dimensions, i.e., height and width. Heterogeneous walls, on the other hand, have varying material composition along either or both dimensions. Examples of heterogeneous wall are cinderblock wall, reinforced wall, and drywall (wood with air gaps covered with plaster). Electromagnetic simulation tool such as Finite Difference Time Domain (FDTD) has commonly been used to model the radar returns from these wall types as it can predict accurately the fast-fading phenomenon caused by the inhomogeneities of the wall. However, FDTD is time consuming and computation intensive in modeling an entire large TWRI scene. In this paper, we use ray-tracing technique for simulations and consider a heterogeneous wall as a dielectric slab with relative permittivity varying as a function of the antenna position.

1) *Heterogeneous Wall*: Let us consider a lossless heterogeneous wall of thickness d to be modeled as a uniform dielectric slab in which the dielectric properties vary as a function of position of the antenna. The reflection and transmission behavior of an electromagnetic plane wave incident on the wall can be found using Maxwell's equations [20]. The total reflection coefficient $\Gamma(k_m, \epsilon_n)$ of the received signal at the n -th antenna location and m -th frequency can be written as

$$\Gamma(k_m, \epsilon_n) = \frac{\rho_n(1 - \exp(-2j\sqrt{\epsilon_n}k_md))}{1 - \rho_n^2 \exp(-2j\sqrt{\epsilon_n}k_md)}, \quad (10)$$

where ϵ_n is the relative permittivity of the wall at the n -th antenna location, $k_m = \omega_m/c$ is the m -th wave number and ρ_n is the local Fresnel reflection coefficient given by

$$\rho_n = \frac{1 - \sqrt{\epsilon_n}}{1 + \sqrt{\epsilon_n}}. \quad (11)$$

The radar signal backscattered from the wall received at the n -th antenna can be approximately written as

$$S_w(m, n) = \frac{G\lambda}{8\pi} \frac{\exp(-j2k_m z_o)}{z_o} \Gamma(k_m, \epsilon_n), \quad (12)$$

where z_o is the standoff distance from the radar to the wall, λ is the wavelength, G is the antenna gain, and c is the speed of light in free space [10]. For the sake of conciseness, we let

$$\phi(k_m) = \frac{G\lambda}{8\pi} \frac{\exp(-j2k_m z_o)}{z_o}, \quad \text{for } m = 0, \dots, M-1, \quad (13)$$

and denote by \mathbf{b}_n the vector of reflection coefficients at the n -th antenna location:

$$\mathbf{b}_n = [\Gamma(k_1, \epsilon_n), \Gamma(k_2, \epsilon_n), \dots, \Gamma(k_M, \epsilon_n)]^T, \quad \text{for } n = 0, \dots, N-1. \quad (14)$$

The signals backscattered from the wall and received by the N -element array can be arranged into a matrix B , $B \in \mathbb{C}^{M \times N}$, ($M > N$), where each column contains the monochromatic signals received at one antenna location. Using (13) and (14), the matrix B is expressed as

$$B = \Phi[\mathbf{b}_0, \dots, \mathbf{b}_{N-1}], \quad (15)$$

where $\Phi = \text{diag}(\phi(k_0), \dots, \phi(k_{M-1}))$ is a diagonal matrix with its elements on the main diagonal given in (13). The wall eigen-subspace can be obtained by applying an eigendecomposition method such as SVD and identifying the singular vectors containing the wall returns. The rank of the matrix B , i.e., the number of linearly independent columns in the matrix, determines the dimension of the wall subspace. It is clear from (14) and (15) that the columns of the matrix B depend strongly on the relative permittivity of the wall, among other factors. Therefore, if the wall relative permittivity varies across the antenna array, the columns of B will become linearly independent, and thus the wall eigen-subspace will be spanned by multiple singular components.

To illustrate the effect of the relative permittivity on the wall subspace, we consider a heterogeneous wall as a drywall with varying relative permittivity along the antenna array. The drywall is modeled as two parallel dielectric slabs with an air gap. The dielectric constant of the wall is varied from 2 to 2.8 along the array aperture. Let us consider a two-meter array aperture with 50 antennas and each antenna transmitting a stepped-frequency signal with a bandwidth of 2 GHz centered at 2 GHz. The step size is set to 10 MHz to produce 201 monochromatic

signals. The received signals at all antenna locations are arranged into the matrix B given in (15), which can be expressed, using SVD, as

$$B = U\Sigma V^H, \quad (16)$$

where H denotes Hermitian transpose, $U = [\mathbf{u}_1, \dots, \mathbf{u}_M]$ and $V = [\mathbf{v}_1, \dots, \mathbf{v}_N]$ are unitary matrices containing the left and right singular vectors, respectively, and Σ is a rectangular matrix of the same size as B with singular values σ on the diagonal arranging in decreasing order, i.e., $\sigma_1 \geq \sigma_2 \geq \dots \geq \sigma_N \geq 0$. Figure 2 illustrates the image of the scene and the singular values of B . Since there is no target behind the wall, the received signal consists of wall reflections only, see Fig. 2(a). Therefore, all the nonzero singular values in Fig. 2(b) are due to wall reflections. This shows that varying the wall relative permittivity results in a wall subspace spanned by several singular vectors. Next, we investigate the subspace of a real (i.e., not simulate) drywall.

A ground-based stepped-frequency TWRI system was used to interrogate a drywall made of two types of materials: plywood and gypsum wallboard. Details of the TWRI system and the drywall will be given in Section V. The received signals are used to analyze the subspace of the drywall. Figure 3 shows the formed image and the singular values of the data matrix. Figure 3(a) shows an image with strong wall clutter from the drywall in an empty scene and Fig. 3(b) depicts the singular values. Results from the simulation and real experimental data confirm that reflections backscattered from a heterogeneous wall reside in a multi-dimensional subspace spanned by several singular vectors.

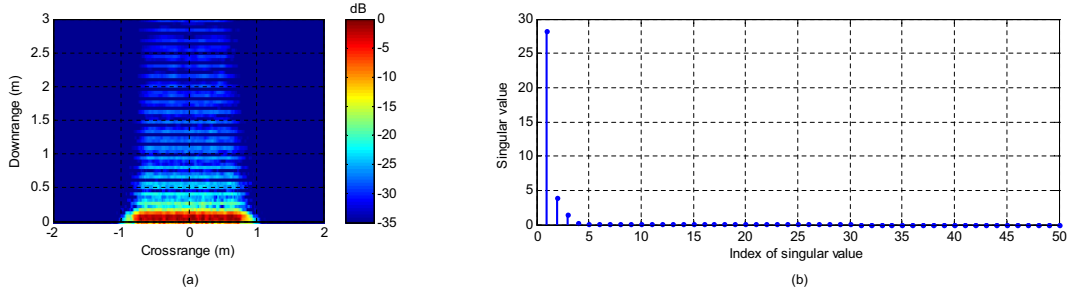


Fig. 2. A simulated empty scene containing a heterogeneous wall: (a) image of the scene obtained using DS beamforming and (b) singular values of the matrix B .

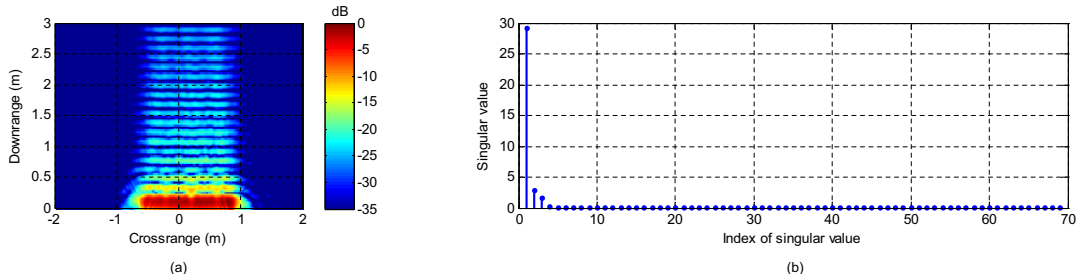


Fig. 3. A real empty scene containing a drywall wall: (a) image of the scene obtained using DS beamforming and (b) singular values of the matrix B .

2) *Homogeneous Wall*: For a lossless homogeneous wall, the relative permittivity is constant across the wall plane, $\epsilon_n = \epsilon$. Thus, the total reflection coefficient is given by

$$\Gamma(k_m) = \frac{\frac{1-\sqrt{\epsilon}}{1+\sqrt{\epsilon}}(1 - \exp(-2j\sqrt{\epsilon}k_md))}{1 - \left(\frac{1-\sqrt{\epsilon}}{1+\sqrt{\epsilon}}\right)^2 \exp(-2j\sqrt{\epsilon}k_md)}. \quad (17)$$

It follows from (13) and (17) that the columns of B are identical, i.e., $\Phi \mathbf{b}_0 = \Phi \mathbf{b}_1 = \dots = \Phi \mathbf{b}_{N-1}$, leading to a matrix of rank one. Even the homogeneous wall is lossy, so long as the dielectric constant does not change along the wall plane, the homogeneous wall subspace is one-dimensional— provided there is perfect alignment of the array with the wall and the wall is of uniform thickness.

If the antenna array is not perfectly aligned with the wall, each antenna element will be at a different standoff distance z_n from the wall. Therefore, the term $\varphi(k_m)$ in (13) becomes dependent also on the antenna location.

$$\phi(k_m, z_n) = \frac{G\lambda \exp(-j2k_m z_n)}{8\pi z_n}. \quad (18)$$

As the diagonal matrix $\Phi_n = \text{diag}(\phi(k_0, z_n), \dots, \phi(k_{M-1}, z_n))$, $n \in [0, N-1]$, is related to the antenna location, it varies across the antenna array, i.e., $\Phi_0 \neq \Phi_1 \neq \dots \neq \Phi_{N-1}$; thus, the rank of the matrix B is no longer one. This implies that the homogeneous wall subspace is multi-dimensional. To investigate the effect of antenna misalignment on the wall subspace, we perform several simulations with different degree of perturbations in the antenna standoff distance. A subspace distortion factor is computed as a function of the perturbations in the standoff distance. Ideally, a homogeneous wall subspace is spanned by the first singular vector associated with the most dominant singular value. Perturbations in the remaining singular values, due to the antenna displacements, are considered as subspace distortions. Mathematically, we define the subspace distortion factor δ_s as the sum of the square of normalized singular values with respect to the most dominant singular value σ_1 ,

$$\delta_s = \sum_{i=2}^N \left(\frac{\sigma_i}{\sigma_1} \right)^2, \quad (19)$$

where σ_i is the i -th singular value. Suppose that for each antenna, the standoff distance is set to 1 m and is varied by adding a small random value drawn in the range $[0, 1]$ cm. In terms of the wavelength of the center frequency, λ_0 , the perturbation range is $[0, \lambda_0/15]$, where $\lambda_0 = 15$ cm based on a center frequency of 1.5 GHz. Figure 4(a) illustrates the variations of the subspace distortion factor of a homogenous wall as a function of the perturbations in the standoff distance. Figure 4(b) shows the singular values of the wall subspace for an antenna displacement of 0.1 cm from the standoff distance. Clearly, there is more than one dominant singular value, indicating that the homogeneous wall subspace is spanned by multiple singular vectors.

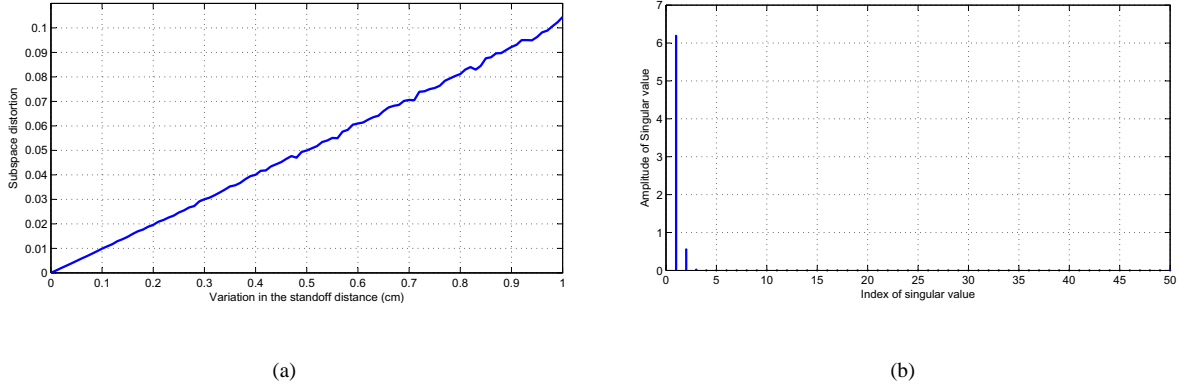


Fig. 4. Perturbation analysis in the antenna standoff distance: (a) subspace distortion factor as a function of the variation in the standoff distance and (b) singular values at a perturbation of 1mm in the standoff distance.

If the wall exhibits nonuniform thickness along the array, the total reflection coefficient will be a function of the antenna location; it is written as

$$\Gamma(k_m, d_n) = \frac{\frac{1-\sqrt{\epsilon}}{1+\sqrt{\epsilon}}(1 - \exp(-2j\sqrt{\epsilon}k_md_n))}{1 - \left(\frac{1-\sqrt{\epsilon}}{1+\sqrt{\epsilon}}\right)^2 \exp(-2j\sqrt{\epsilon}k_md_n)}. \quad (20)$$

Based on (20), the columns of the second term of (15) differ from each other, i.e., $\mathbf{b}_0 \neq \mathbf{b}_1 \neq \dots \neq \mathbf{b}_{N-1}$. Thus, the columns of B become linearly independent and B is a high-rank matrix. To illustrate this, at each antenna location, we alter the wall thickness d by adding a small random value in the range $[0, 1]$ mm. The subspace distortion factor is computed while varying the degree of perturbation in the wall thickness. Figure 5 illustrates the effect of wall thickness perturbations on the wall subspace. Figure 5(a) displays the subspace distortion factor as a function of the wall thickness perturbations. Figure 5(b) shows the singular values for a perturbation of 0.1 mm, which corresponds to a subspace perturbation factor of 0.006.

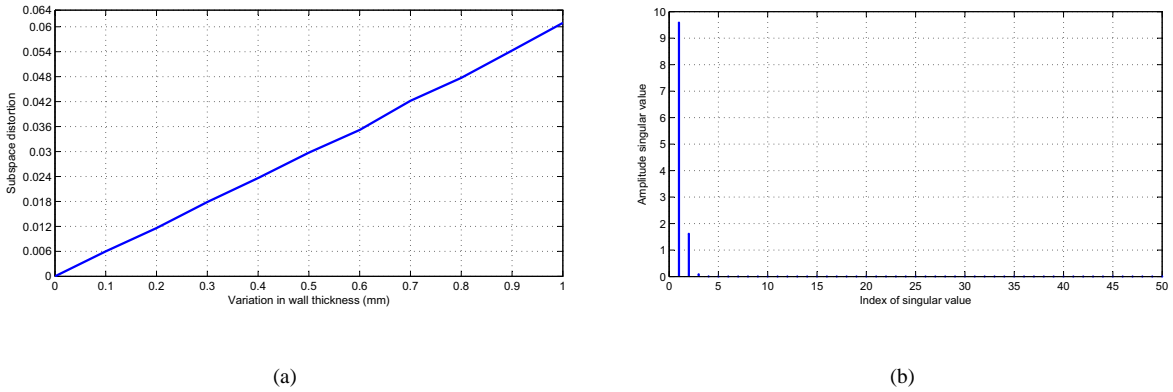


Fig. 5. Perturbation analysis in the wall thickness: (a) subspace distortion factor as a function of the variation in the wall thickness and (b) singular values at a perturbation of 0.1mm.

To summarize, the wall returns are not necessarily characterized by a single singular vector, but can be spanned by multiple singular vectors. There are several factors that affect the dimension of the wall subspace, namely, the wall electromagnetic characteristics, the wall thickness uniformity, and the configuration of the antenna array. Next, we also analyze the target subspace for point-like and extended targets.

B. Target Eigen-Subspace

In this section, we analyze the eigen-subspace of point-like and extended targets. Firstly, we consider a point-like target with frequency-dependent reflection coefficient $\sigma(\omega_m)$ located at the location (z'_p, x'_p) behind a lossless homogeneous wall. The transceiver transmits a perpendicularly polarized wave that is propagated at an oblique angle through the wall. The target signal received at the n -th antenna can be written as [21]:

$$S_t(m, n) = \frac{G\lambda}{4\pi} \frac{T^4(n)}{(R_{n,air1} + R_{n,w} + R_{n,air2})^2} \frac{\cos^2(\phi_n)}{\cos^2(\varphi_n)} \sigma(\omega_m) \epsilon \exp(-j\omega_m \tilde{\tau}_n(z'_p, x'_p)), \quad (21)$$

where $T(n)$ is the transmission coefficient received at the n -th antenna given by

$$T(n) = \frac{2 \cos(\varphi_n)}{\cos(\varphi_n) + \sqrt{\epsilon} \cos(\phi_n)}. \quad (22)$$

An extended target is simulated by assuming that its reflection coefficient is frequency independent and constant over its spatial 2-D extent, $\sigma(\omega_m) = \sigma$. Let d_z and d_x denote the width and length of the extended target, respectively. The signal reflected by an extended target located at (z'_p, x'_p) can be written as [19]:

$$\begin{aligned} S_t(m, n) &= \sigma \vartheta_n \int_{-d_z/2}^{d_z/2} \exp\left(\frac{2\omega_m}{c} \cos(\theta_n)(z'_p + z)\right) dz \cdot \int_{-d_x/2}^{d_x/2} \exp\left(-\frac{2\omega_m}{c} \sin(\theta_n)(x'_p + x)\right) dx \\ &= 4\sigma \vartheta_n d_x d_z \cdot \text{sinc}\left(\frac{\omega_m \cos(\theta_n) d_z}{c}\right) \text{sinc}\left(\frac{\omega_m \sin(\theta_n) d_x}{c}\right) \exp\left(-j \frac{2\omega_m}{c} (z'_p \cos(\theta_n) - x'_p \sin(\theta_n))\right), \end{aligned} \quad (23)$$

where $\text{sinc}(x)$ is the Sinc function and ϑ_n given by

$$\vartheta_n = \frac{G\lambda}{4\pi} \frac{T^4(n)}{(R_{n,air1} + R_{n,w} + R_{n,air2})^2} \frac{\cos^2(\phi_n)}{\cos^2(\varphi_n)}. \quad (24)$$

The target signals received at each antenna location are arranged into a column of the matrix B :

$$B = [s_0, \dots, s_{N-1}], \quad (25)$$

where $s_n = [S_t(0, n), \dots, S_t(M-1, n)]^T$, $n \in [0, N-1]$. In (21) and (23), the incident and refracted angles, φ and ϕ , as well as the two-way propagation delay from the antenna to the target, $\tilde{\tau}$, are dependent on the antenna location. In near field imaging, these quantities are expected to vary significantly from one antenna location to another, leading to linearly independent columns of the matrix B given in (25). Therefore, the rank of B is dependent on the target location. For example, a target placed at the center of the array will yield a reduced rank of B since the signal propagation delays from the antennas in the left half of the array are the same as those in the right half of the array, i.e., $\tilde{\tau}_1 = \tilde{\tau}_N, \tilde{\tau}_2 = \tilde{\tau}_{N-1}$, etc. In our recent study [17], we have shown that reflections from a point-like target span a multi-dimensional subspace, due to several factors that can influence the target reflections and the signal propagation delays, e.g., the target location and the configuration of the antenna array. Here, we

additionally analyze the target subspace of an extended target, and a combination of point-like and extended targets. It is evident from (21) that the signal backscattered from a point-like target is a function of the two-way propagation delay, which, in turn, is related to the distance from the antenna to the target. For an extended target, the received signal is a function of not only the two-way propagation delay, but also the spatial extent of the target. A slight change in these parameters, namely the two-way propagation delay and the spatial extent of the target causes the columns of B to be different from each other. For illustration, we consider a point-like and an extended target placed at locations $(-1.38, 1.16)$ m and $(1.05, 2.13)$ m in free space, respectively. Figure 6 presents images of different target types, Figs. 6(a)–(c), and the singular values of B associated with these targets, Figs. 6(d)–(f). On the other hand, having two targets and placing them far apart from each other increases the number of non-zero singular values, see Fig. 6(f).

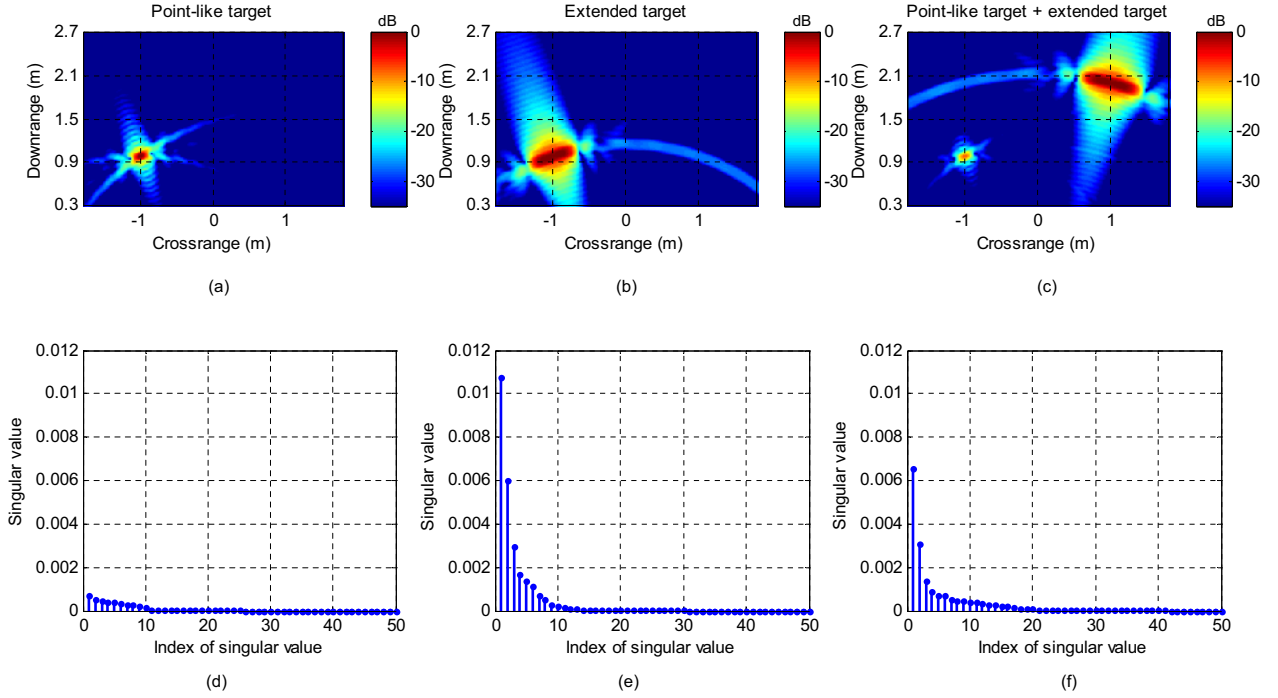


Fig. 6. Formed images and singular values of matrix B for different target types in a free-space scene: (a) image of a point-like target, (b) singular values of a point-like target, (c) image of an extended target, (d) singular values of an extended target, (e) image of combined point-like and extended targets, and (f) singular values of combined point-like and extended targets.

Next, we investigate the subspace dimension of an extended target under two imaging scenarios: short-range and long-range, where the target is placed close to or far from the radar system. In the former, the viewing angle θ_n of the antenna varies considerably across the array aperture, causing the distance traveled by the signal from each antenna to the target to be different. Based on the extended target signal model given in (23), it is clear that the target signal is related to θ_n , and therefore, the number of linearly independent columns in the matrix B increases when the viewing angle varies markedly across the array aperture. On the other hand, for a long-range

target, the changes in the viewing angle across the antenna array are much smaller, resulting in almost the same distance between each antenna element and the target; therefore, the target subspace is narrower compared to that of a short-range target. To illustrate this, an extended target is placed at two different locations: a short range at $(-1, 1)$ m and a long-range at $(-1, 5.5)$ m. The formed images and the singular values for both cases are shown in Fig. 7. Figures 7(a) and (b) depict, respectively, the formed image and the singular values of a near target, whereas Figs. 7(c) and (d) show the image and singular values of a distant target. The difference in the number of nonzero singular values between Figs. 7(b) and (d) confirms that the subspace of a distant target is narrower than that of a near target.

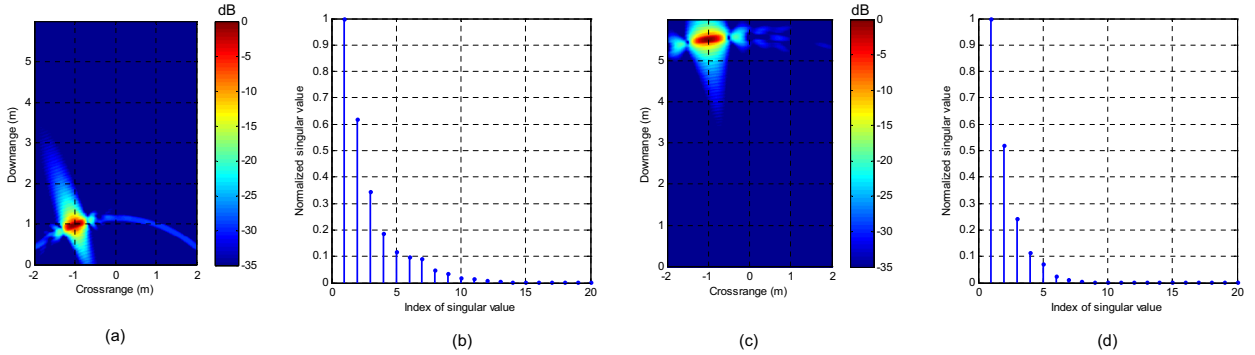


Fig. 7. Formed image and singular values of two different imaging ranges: (a) image of a near target, (b) singular values of a near target, (c) image of a distant target, and (d) singular values of a distant target. For visualization, only the first 20 singular values are shown.

In summary, the target returns do not span a one-dimensional subspace as reported in some existing literatures [13]–[15], but a multi-dimensional subspace, dependent on several factors. These factors include, among others, the target location, the target type, the number of targets in the scene, and the antenna array configuration. In the following subsection, we investigate the eigen-structure of the combined wall and target returns.

C. Wall-Target Eigen-Subspace

In the above analysis, we have shown that the wall subspace can be multi-dimensional even when the wall is homogeneous. Furthermore, when considering the data in frequency and space, the target reflections span a multi-dimensional subspace. Here, we investigate the eigen-structure of combined wall and target returns. By including reflections from both the wall and the target, the received signal can be expressed as a superposition of the wall and target returns:

$$S(m, n) = S_w(m, n) + S_t(m, n), \quad (26)$$

where $S_w(m, n)$ is the wall returns and $S_t(m, n)$ is the target returns. Since the wall reflections are relatively stronger than the behind-the-wall target reflections, it is assumed that the wall returns mostly lie in a subspace spanned by the singular vectors associated with the dominant singular values. Therefore, by discarding the singular vectors associated with the dominant singular values, the wall returns can be removed from the radar signals. For

demonstration, we simulate a scene with two extended targets placed behind a non-uniform lossless homogeneous wall at coordinates $(-0.66, 0.77)$ and $(0.40, 0.98)$ m. A 0.15 m thick wall with a dielectric constant of 5.5 is placed at a standoff distance of 1 m. By using SVD, the matrix B , which comprises the frequency-space measurements, is decomposed into a set of N singular components:

$$B = \sum_{i=1}^N \sigma_i \mathbf{u}_i \mathbf{v}_i^H. \quad (27)$$

Figure 8 illustrates the formed images of the two targets behind the wall. Figure 8(a) shows the image formed by using all N singular components in (27). Clearly, the wall reflections and ringing effects dominate the image and obscure the targets. Figure 8(b) presents the image after removing the first leading singular component, and Fig. 8(c) shows the image without the first two dominant singular components. Removing just the first dominant singular component eliminates most of the wall reflections and the ringing effects. The target image is further enhanced by removing the second singular component, Fig. 8(c).

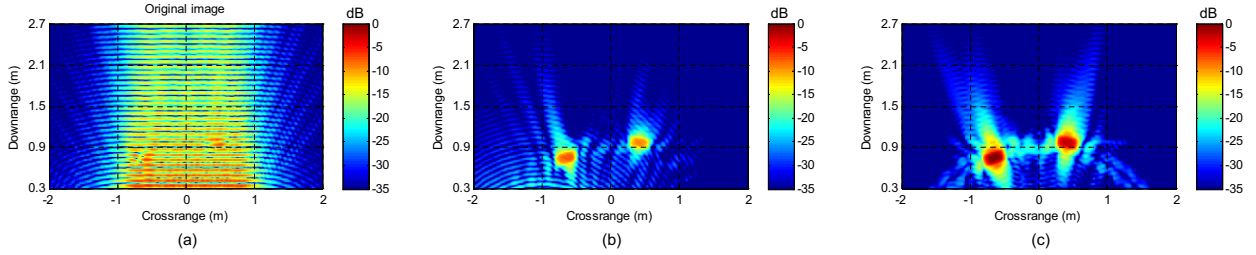


Fig. 8. Image of a scene with two extended targets placed behind a homogeneous wall: (a) image of targets and wall, (b) image without the first dominant singular component, and (c) image without the first two leading singular components.

Because of misalignment of antenna elements and non-uniformity of wall thickness, the homogeneous wall returns reside in a high dimensional subspace, spanned by more than two singular vectors. Some of the wall singular vectors are associated with the non-dominant singular values, which may be interleaved among the target singular values. To identify the singular vectors characterizing the wall returns, we propose a simple procedure. From (27), the matrix B consists of a weighted sum of N singular components, where each singular component is given by the outer product of a pair of left and right singular vectors multiplied by its corresponding singular value. Let B_i denote the i -th singular component, given by

$$B_i = \sigma_i \mathbf{u}_i \mathbf{v}_i^H = [\mathbf{g}_{i,1}, \dots, \mathbf{g}_{i,N}], \quad (28)$$

where $\mathbf{g}_{i,j}$ denotes the j -th column vector of the matrix B_i . The range profile associated with the i -th singular component can be computed as

$$\mathbf{r}_i = \sum_{k=1}^N \text{IFFT}(\mathbf{g}_{i,k}), \quad (29)$$

where IFFT denotes the inverse fast Fourier transform. The main peak in a range profile is used to indicate whether the singular component contains the wall or target returns, depending on the peak location with respect to the

antenna standoff distance. Figure 9 shows the range profiles of the first eight singular components. The range profiles depicted in Figs. 9(a)–(c) show the first three singular components consist of the wall returns since the main peaks of their associated range profiles are located at around the standoff distance of the antenna array, which is 1 m. The range profile of the fourth singular component has peaks around 2 m, where the target are located, see Fig. 9(d). The small difference between the location of the peak in the range profile and the actual target range is due to the wall attenuation. Figures 9(e) and (f) present the range profiles of the fifth and the sixth singular components, indicating that they also contain the target returns. In Fig. 10(g), the main peak is around the wall location, meaning that the seventh singular component consists of residual wall returns. The last range profile in Fig. 10(h) clearly belongs to target. Figure 10 present images obtained from a subset of selected singular components. The image in Fig. 10(a) is reconstructed from the seventh singular component and that depicted in Fig. 10(b) is obtained from the combination of the 4, 5, 6, and 8 singular components. The simulation results show that apart from the first few dominant singular vectors, there are other non-dominant singular vectors that capture the wall returns. Though the non-dominant wall singular vectors are interleaved among the target singular vectors, their associated range profiles look similar, i.e., their main peaks are located around the wall position. In the next section, we propose a technique to estimate the wall subspace, and introduce a subspace projection method for mitigating the wall returns from the radar signals.

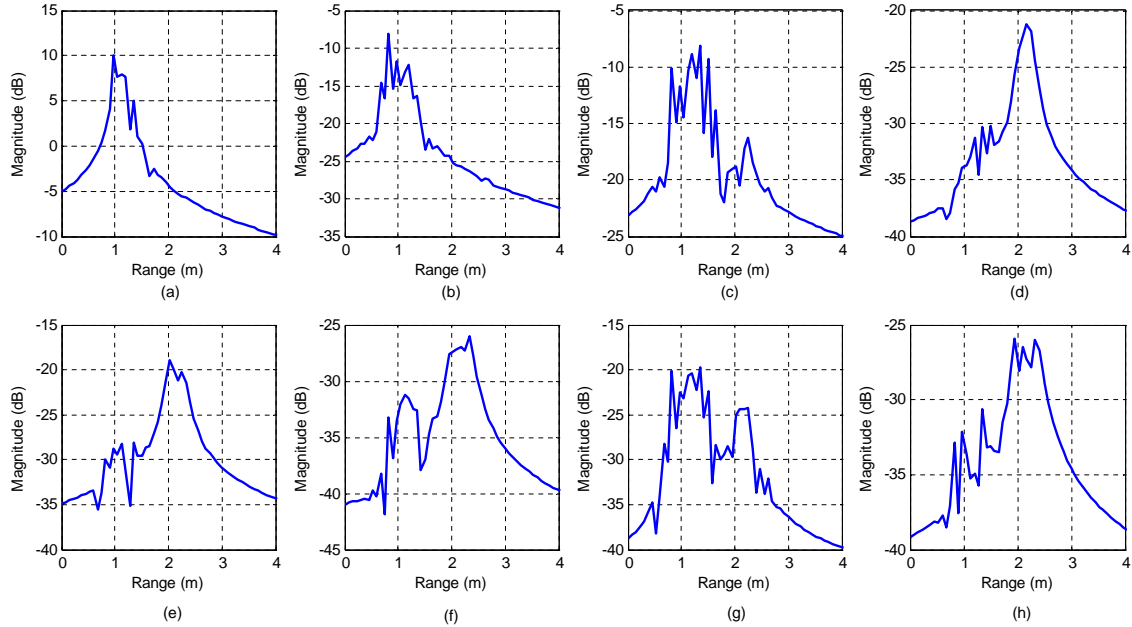


Fig. 9. The range profiles of the first 8 dominant singular components (ECs): (a) range profile of the EC-1, (b) range profile of the EC-2, (c) range profile of the EC-3, (d) range profile of the EC-4, (e) range profile of the EC-5 (f) range profile of the EC-6, (g) range profile of the EC-7, and (h) range profile of the EC-8.

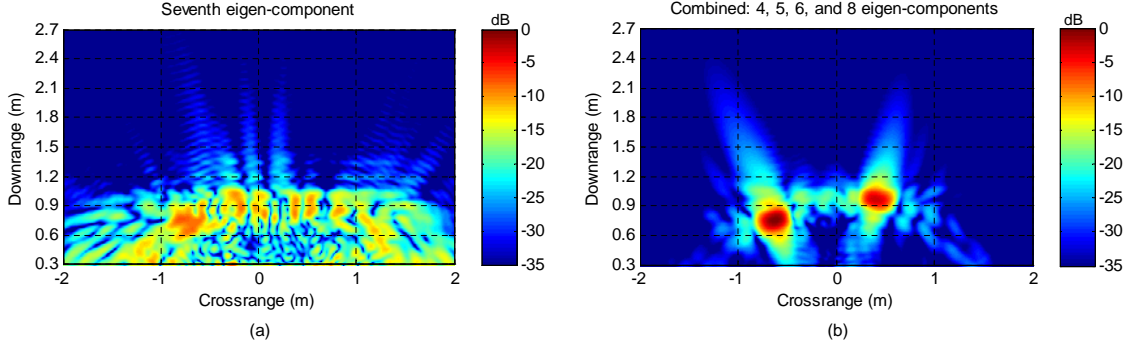


Fig. 10. Images formed using a subset of singular components: (a) image obtained from the 7th singular component and (b) image obtained from singular components 4, 5, 6, and 8.

IV. WALL CLUTTER MITIGATION METHOD

The proposed wall clutter mitigation method is based on the assumption that the wall returns are relatively stronger than the target returns and they reside in separate subspaces. Therefore, SVD is used to decompose the matrix B :

$$B = \sum_{i \in \mathcal{W}} \sigma_i \mathbf{u}_i \mathbf{v}_i^H + \sum_{i \in \mathcal{T}} \sigma_i \mathbf{u}_i \mathbf{v}_i^H + \sum_{i \in \mathcal{N}} \sigma_i \mathbf{u}_i \mathbf{v}_i^H, \quad (30)$$

where \mathcal{W} , \mathcal{T} , and \mathcal{N} are the sets of indices for wall, target, and noise singular vectors, respectively. However, not all wall singular components will be associated with the dominant singular values. While it is expected that the strong wall reflections will be represented by the first few singular vectors associated with the dominant singular values, some weak components of the wall returns may reside in a subspace spanned by other singular vectors associated with non-dominant singular values. Therefore, we propose a method for estimating the wall subspace followed by a subspace projection method for mitigating the wall returns from the radar signals.

A. Wall Subspace Estimation

The proposed estimation method for wall subspace is based on the assumption that the strong reflections from the front and back of the wall are captured by the first few dominant singular components. In [22], similar assumption was made to estimate the time delay of UWB radar signals backscattered from a wall. Herein, we first estimate the wall range, i.e., the distance from the antenna to the back of the wall from the range profiles of the dominant singular components. Then, we classify the remaining singular components into the wall and target subspace, based on their range profiles. The indices of the singular vectors forming the wall singular components are stored in the index set \mathcal{W} . Let η denote the wall range. If the standoff distance z_o and the wall thickness d are known, the wall range can be approximated as

$$\eta \approx (d\sqrt{\epsilon} + z_o). \quad (31)$$

In practice, the exact values of the wall parameters are not readily available. Therefore, we determine the wall range from the range profiles associated with the dominant singular vectors. To determine the leading singular vectors associated with the wall, we apply a threshold technique to segment the singular value spectrum into two classes, one of which is the dominant wall singular values. Suppose the range of singular values is $[0, \sigma_{max}]$. Given a threshold $\tau \in [0, \sigma_{max}]$, the singular value spectrum can be partitioned into two classes: $\mathcal{C}_w = \{\sigma_i \leq \tau\}$ and $\mathcal{C}_t = \{\sigma_i > \tau\}$. Here, we employ Otsu's method [23], which computes the optimum threshold τ^* by maximizing the between-class variance:

$$\Sigma_0 = P_w(\mu_w - \mu_0)^2 + P_t(\mu_t - \mu_0)^2, \quad (32)$$

where P_w and P_t are the class probabilities, μ_w and μ_t are the class means, and μ_0 is the total mean of the classes. For more details on how to determine the optimum threshold of Otsu's method, the reader is referred to Appendix A.

After determining the optimum threshold, τ^* , Eq. (29) is used to compute the range profiles associated with the singular values in the class \mathcal{C}_w . Let ρ_i denote the range of the main peak in the range profile associated with the i -th singular value in the class \mathcal{C}_w . The wall range η can be estimated as

$$\eta^* = \max_i(\rho_i). \quad (33)$$

From the estimated wall range, we can now identify the remaining wall singular components and determine the singular vectors spanning the wall subspace. We classify a singular component belonging to the wall class when the main peak ρ of its associated range profile is within the wall range η^* . This classification is performed on all singular components of B and the indices of the wall singular vectors are stored in the index set \mathcal{W} .

B. Wall Clutter Mitigation

After identifying the wall subspace, the wall returns can be removed by projecting the radar signals onto the subspace orthogonal to the wall subspace. Similarly, the noise can be removed by projecting the radar signals onto the subspace orthogonal to the noise subspace. First, the radar signal is preprocessed to remove the common signal across the array aperture. Let \tilde{B} be the matrix obtained after subtracting the mean vector from each column of B ,

$$\tilde{B} = B - \mathbf{m}\mathbf{e}^T, \quad (34)$$

where \mathbf{m} is the mean of the columns of B and $\mathbf{e}^T = [1, \dots, 1]$, $\mathbf{e} \in R^N$, is a row vector of 1. Using SVD, the matrix \tilde{B} can be expressed as

$$\tilde{B} = \tilde{U}\tilde{\Sigma}\tilde{V}^H. \quad (35)$$

where $\tilde{U} = [\tilde{\mathbf{u}}_1, \dots, \tilde{\mathbf{u}}_M]$, $\tilde{V} = [\tilde{\mathbf{v}}_1, \dots, \tilde{\mathbf{v}}_N]$, and $\tilde{\Sigma}_{i,i} = \tilde{\sigma}_i$. By summing the outer product of the pair of singular vectors in the index set \mathcal{W} , the wall subspace is given by

$$\mathbf{P}_w = \sum_{i \in \mathcal{W}} \tilde{\mathbf{u}}_i \tilde{\mathbf{v}}_i^H. \quad (36)$$

The subspace orthogonal to the wall subspace is computed as

$$\mathbf{P}_w^\perp = I - \mathbf{P}_w \mathbf{P}_w^H, \quad (37)$$

where I denotes the identity matrix. To mitigate the wall returns, the matrix \tilde{B} is projected onto the orthogonal subspace:

$$\hat{B} = \mathbf{P}_w^\perp \tilde{B}. \quad (38)$$

After removing the wall returns, the modified \hat{B} matrix is further processed to remove the noise subspace. The modified \hat{B} is projected onto the subspace orthogonal to the noise subspace,

$$\mathbf{P}_n^\perp = I - \mathbf{P}_n \mathbf{P}_n^H, \quad (39)$$

where $\mathbf{P}_n = \sum_{i \in \mathcal{N}} \hat{\mathbf{u}}_i \hat{\mathbf{v}}_i^H$ is the noise subspace. The pair of left and right singular vectors, i.e., $\hat{\mathbf{u}}$ and $\hat{\mathbf{v}}$ are obtained from the SVD of \hat{B} . Since the noise is characterized by singular vectors associated with small singular values, there are several methods to determine the noise subspace. Akaike Information Criterion (AIC) and Minimum Description Length (MDL) methods are two commonly used methods to estimate the noise subspace [16]. Herein, we employ one of the information theoretic criteria methods to determine the noise subspace. The AIC is given by

$$\text{AIC}(i) = N \log \left(\frac{\left((1/(M-i)) \sum_{m=i+1}^M \sigma_m \right)^{M-i}}{\prod_{m=i+1}^M \sigma_m} \right) + i(2M-i), \quad (40)$$

where σ_i is the i -th singular value of \hat{B} . Similarly, the MDL is given by

$$\text{MDL}(i) = N \log \left(\frac{\left((1/(M-i)) \sum_{m=i+1}^M \sigma_m \right)^{M-i}}{\prod_{m=i+1}^M \sigma_m} \right) + \frac{1}{2} i(2M-i) \log(N). \quad (41)$$

The number of singular values belonging to the noise class is determined by minimizing the AIC or MDL. Once the wall and noise subspaces are computed, the new matrix, B^* , free from the wall and noise contributions is written as

$$B^* = \mathbf{P}_n^\perp (\mathbf{P}_w^\perp \tilde{B}) = \mathbf{P}_t \tilde{B}, \quad (42)$$

where $\mathbf{P}_t = \mathbf{P}_n^\perp \mathbf{P}_w^\perp$ is the target subspace projection operator. Finally, to form an image of the scene, DS beamforming is applied to the new matrix B^* .

The proposed method is initially tested on simulated data based on the same radar setting as the previous simulations. Here, two different types of walls are investigated: lossless and lossy homogeneous walls. The relative wall dielectric parameters are permittivity $\epsilon = 5.5 - j0.18$, and conductivity $\sigma = 5.01\text{E-}2$ S/m. The calculation of the reflection and transmission coefficients of a lossy homogeneous wall are given in the Appendix B. To measure the performance of the wall clutter mitigation method, the improvement factor (IF) in terms of the target-to-wall-clutter ratio (TWCR) is evaluated

$$\text{IF} = 10 \log \left(\frac{\text{TWCR}_o}{\text{TWCR}_i} \right), \quad (43)$$

where TWCR_o and TWCR_i are, respectively, the target-to-wall-clutter ratios of the formed image with and without the use of the wall mitigation method. The TWCR of a radar image is calculated as

$$\text{TWCR} = \frac{\frac{1}{N_t} \sum_{(z,x) \in A_t} |I(z,x)|}{\frac{1}{N_c} \sum_{(z,x) \in A_c} |I(z,x)|}, \quad (44)$$

where A_t is the target region, A_c is the wall clutter region, N_c and N_t are, respectively, the number of pixels in the wall clutter and target regions. To measure the quality of the target image, the target power ratio (TPR) is computed and is given by

$$\text{TPR} = \frac{\mathcal{P}_j}{\mathcal{P}_0}, \quad (45)$$

where $\mathcal{P}_0 = \frac{1}{N_t} \sum_{(z,x) \in A_t} |I_0(z,x)|$, $\mathcal{P}_j = \frac{1}{N_t} \sum_{(z,x) \in A_t} |I_j(z,x)|$, and $I_0(z,x)$ and $I_j(z,x)$ denote, respectively, the formed image after background subtraction and the formed image after removing the first j dominant singular components from the matrix B . Figure 11 shows images formed by DS beamforming before and after wall clutter mitigation. Figures 11(a) and (b) illustrate the images before and after the use of the proposed method for a scene with a lossless homogenous wall, whereas Figs. 11(c) and (d) depict images for a scene with a lossy homogeneous wall. In both scenes, two targets are placed behind the wall. The simulation results clearly show that the proposed method can effectively suppress the wall clutter for both wall types. Table I lists the improve factor (IF) and the target power ratio (TPR) of the formed images after wall clutter mitigation. The proposed subspace projection method in conjunction with the wall subspace estimation technique achieves an IF of 12.18 dB when the wall is lossless and 11.86 dB when the wall is lossy. The wall subspace estimated by the proposed method is spanned by singular vectors with indices of 1, 2, 3, and 7. In terms of TPR, the proposed method achieves a TPR of -0.06 dB for lossless wall and -0.12 dB for lossy wall. When the dominant singular components are removed without the use of the proposed wall subspace estimation method, the IFs of the formed images are presented as follows. After the removal of the dominant singular component from the matrix B , the IF of the formed image is 4.55 dB for lossless wall and 4.45 dB for lossy wall. Discarding the first two leading singular components improves the IF of the image to 11.49 dB for lossless and 10.70 dB for lossy walls. By removing the first three singular components, we achieve an IF of 12.16 dB for lossless and 11.81 dB for lossy wall. However, when we remove the first four singular components from the matrix B , the IF of the formed images decreases slightly for both lossless (11.17 dB) and lossy (11.33 dB) walls. The TPR of the formed target image also decreases markedly when the first four singular components are discarded. Considering the wall subspace spanned by the first four singular vectors gives a TPR value of -2.26 dB for lossless wall and -2.36 dB for lossy wall, whereas the TPR of the proposed method is -0.06 dB for lossless and -0.12 dB for lossy walls.

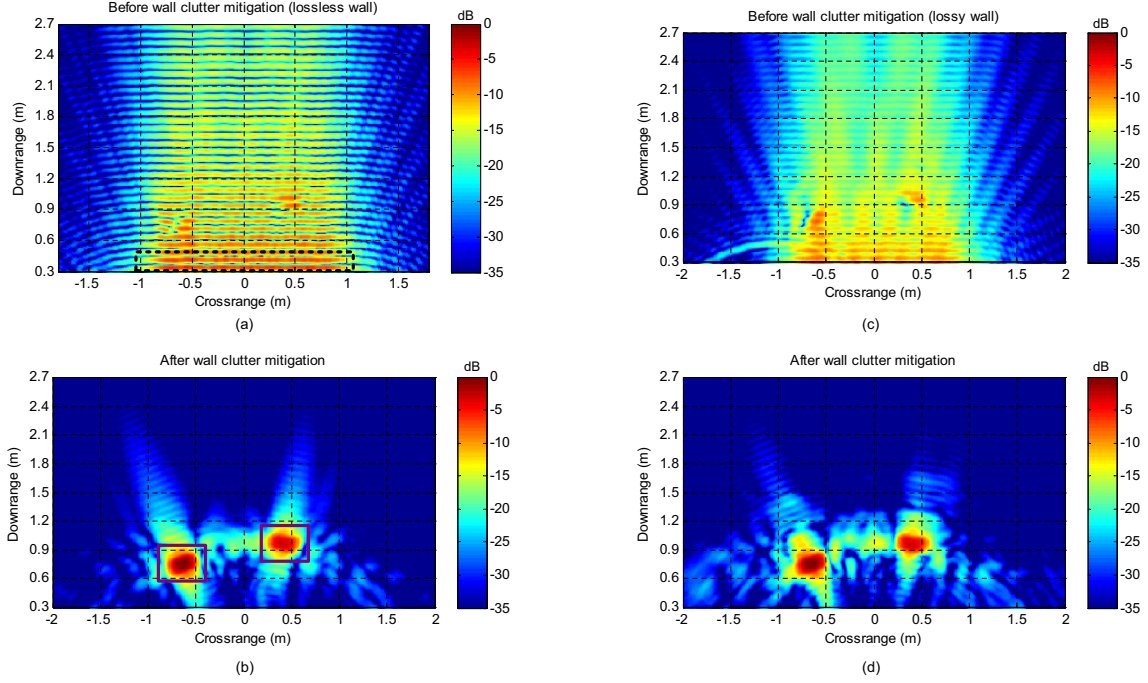


Fig. 11. Images before and after wall clutter mitigation: (a) and (b) images obtained from a lossless homogeneous wall and (c) and (d) images obtained from a lossy homogeneous wall. The dash rectangle in (a) and the solid rectangles in (b) represent the wall clutter and target regions used for computing the TCR of the image.

TABLE I

IMPROVEMENT FACTOR OF THE IMAGE PRODUCED BY THE PROPOSED SUBSPACE PROJECTION METHOD AND THE BASIC SVD-BASED METHOD WITH THE REMOVAL OF DOMINANT SINGULAR COMPONENTS, TESTED ON SYNTHETIC DATA.

	Improvement factor (IF)		Target power ratio (TPR)	
	Lossless wall	Lossy wall	Lossless wall	Lossy wall
Proposed wall clutter mitigation method	12.18 dB	11.86 dB	-0.06 dB	-0.12 dB
Removal of first singular component	4.55 dB	4.45 dB	0.08 dB	0.12 dB
Removal of first two singular components	11.49 dB	10.70 dB	0.003 dB	0.02 dB
Removal of first three singular components	12.16 dB	11.81 dB	-0.04 dB	-0.03 dB
Removal of first four singular components	11.17 dB	11.33 dB	-2.26 dB	-2.36 dB

In a noiseless TWRI scene, we have shown that the proposed wall clutter mitigation method can mitigate the wall returns from the radar signals. The proposed method is further tested under different noise levels, where the simulated radar signals are corrupted by additive white Gaussian noise. The IF of the image formed by the proposed method is computed while varying the signal-to-noise ratio (SNR) of the input signal. Figure 12 shows the IF of the formed image as a function of the SNR of the input signal. The IF of the formed image remains unchanged until the SNR of the input signal decreases to 45 dB. Figure 13 shows examples of radar images obtained from input signal with SNR of 30 dB and 60 dB. Figures 13(a) and (b) illustrates images after mitigating the wall returns from

a lossless homogeneous wall based on an input signal of 30 dB and 60 dB, whereas images depicted in Figs. 13(c) and (d) are from a lossy homogenous wall, respectively. In the next section, the subspace projection method is evaluated on real radar data collected from a ground-based stepped-frequency TWRI system.

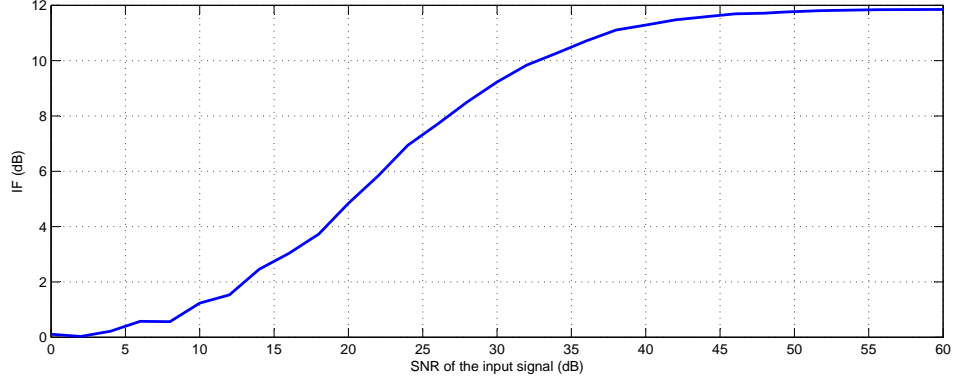


Fig. 12. Improvement factor of the image as a function of the SNR of the input radar signal.

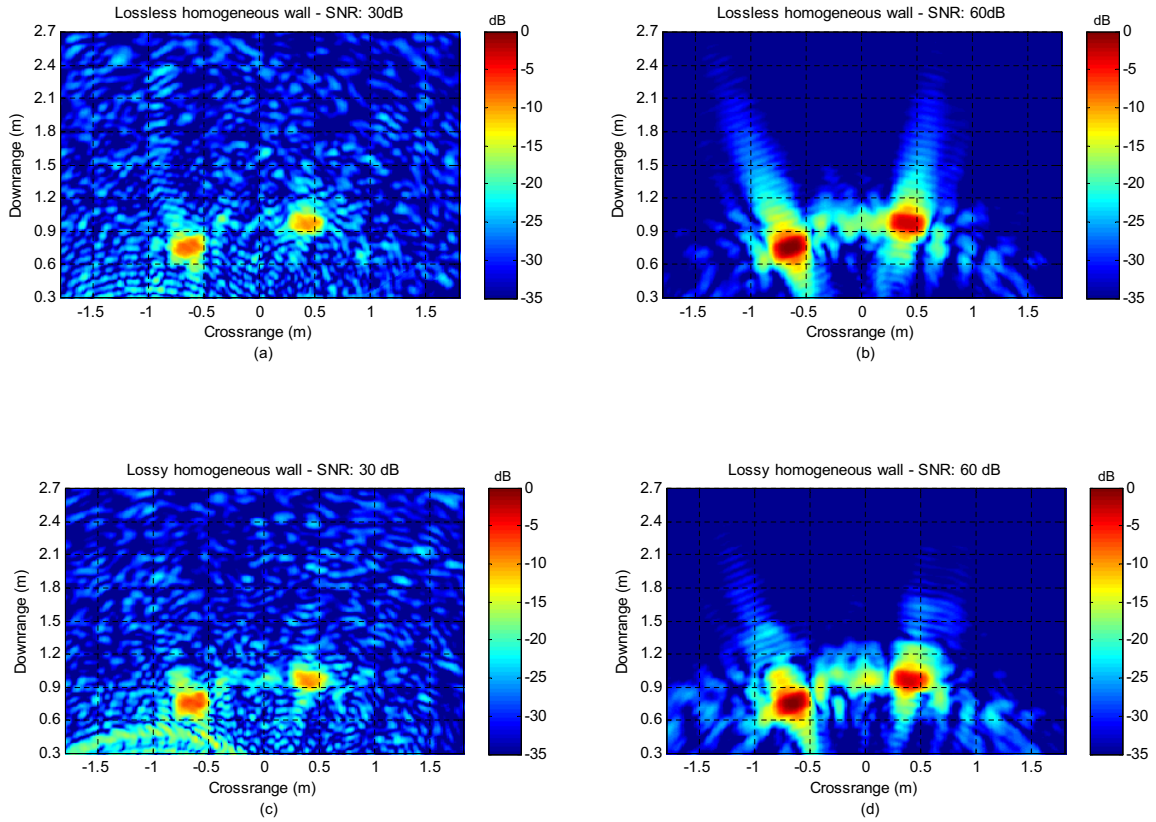


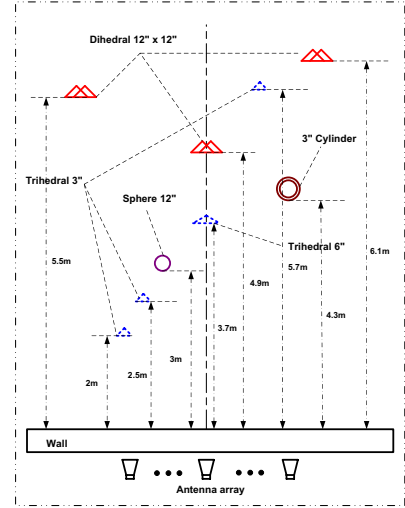
Fig. 13. Examples of images obtained from input signal of different SNRs: (a) and (b) images at SNR of 30 dB and 60 dB for a scene with a lossless wall, and (c) and (d) images at SNR of 30 dB and 60 dB for a scene with a lossy wall. In the scene, two targets are placed behind the wall.

V. EXPERIMENTAL RESULTS

Real data was collected in the Radar Imaging Lab of the Center for Advanced Communications at Villanova University, PA, USA. An Agilent network analyzer, Model ENA 5017B, was used to implement a stepped-frequency waveform for synthesizing a one-dimensional (1-D) and a two-dimensional (2-D) array apertures. A 7.62 by 7.62 meter room with pyramidal foam and laminated polyurethane foam sheet absorbers on the side and back walls was constructed for imaging. For more details about the room setting and the specification of the radar system, the reader is referred to [5].



(a)



(b)

Fig. 14. Image of the second scene: (a) image depicting the nine targets and (b) the ground truth.

A. Experimental Setup

For evaluation purposes, a 1-D and 2-D synthesized array apertures were used for 2-D and 3-D TWRI, respectively. Furthermore, two different TWRI scenarios were designed using two types of walls: a 0.14 m thick solid concrete wall and a 0.127 m thick hollow drywall. The drywall was built from a wooden frame, which is fastened with 0.019 m plywood on one side and 0.016 m gypsum wallboard on the other side. In the first scenario, the radar was placed at a standoff distance of 1.16 m from the concrete wall and a dihedral was positioned at 2.1 m behind the wall. An array aperture of length 1.2446 m was synthesized with 0.0187 m inter-element spacing, and a stepped-frequency signal covering 0.7 to 3.1 GHz frequency band was used to interrogate the scene. The second scenario involves a scene populated with nine targets of different RCS placed behind the drywall. Figure 14 shows the image of the second scene and its ground-truth. The nine targets in the second scene were three dihedrals, four trihedrals, a sphere and a tophat. Each target was located at a certain height and angular displacement, as shown in Fig. 14(a).

Its location within the scene is given in the ground-truth image depicted in Fig. 14(b). The scene was interrogated by using a 69-element array of length 1.534 m and a stepped-frequency signal with a bandwidth of 1 GHz centered at 2.5 GHz. Table II lists the characteristics of the reflectors used in the two TWRI scenes.

TABLE II
REFLECTORS USED IN THE TWRI EXPERIMENTS.

7.62cm Seam Triangular Plate Trihedrals, RCS = -20.6dBsm
15.2cm Seam Triangular Plate Trihedrals, RCS = -8.5dBsm
30.5cm Square plate Dihedrals, RCS = 11.3dBsm
30.5cm Diameter sphere, RCS = -11.4dBsm
Tophat: 7.62cm cylinder width, 50.8cm cylinder height, 71.1cm circular ground plane diameter

B. Two-Dimensional Through the Wall Radar Imaging

A line array aperture was used to interrogate the above described scenes for 2-D imaging. Before DS beamforming, four different types of wall clutter mitigation methods were used, namely background subtraction, time gating, spatial filtering, and SVD-based methods [13]–[16]. Their formed images are compared with that of the proposed subspace projection method. The methods presented in [13]–[16] are based on the SVD of the beamformed image instead of the matrix B containing the frequency-space measurements. In [13]–[15], the wall clutter was represented by the first eigen-image and the target by the second eigen-image. Riaz and Ghafoor, on the other hand, assumed that the target returns span a multi-dimensional subspace and used information theoretic criteria methods such as AIC or MDL to determine the target subspace [16]. Both SVD approaches are compared with the proposed subspace projection method. In time gating, the stepped-frequency signal is transformed into a range profile. Based on the standoff distance and the wall parameters, the radar returns corresponding to the wall region are set to zero and the range profile is converted back to the frequency domain. For background subtraction, radar signals from an empty scene devoid of targets are subtracted from the radar signals received from the scene populated with target(s), before DS beamforming is applied to reconstruct the target image. Background subtraction represents an ideal scenario, where access to the background scene is available; this is not possible in real scenarios. In spatial filtering, an IIR notch filter is used to remove zero frequency component. The frequency response of the notch filter is defined as

$$H(j\omega) = \frac{1 - \exp(-j\omega)}{1 - a \exp(-j\omega)}, \quad (46)$$

where ω is the angular frequency and $a(< 1)$ is positive constant denoting the width of the filter notch. In our experiments, we define a at the point of achieving maximum IF. The first scene, which has a dihedral behind the concrete wall, was illuminated by the synthesized array aperture, producing a matrix B of size 801×57 , i.e., 801 frequencies and 57 antennas. All five wall clutter mitigation approaches including the proposed subspace projection method were used to suppress the wall returns. Figure 15 illustrates images before and after wall clutter mitigation, using the different wall mitigation techniques.

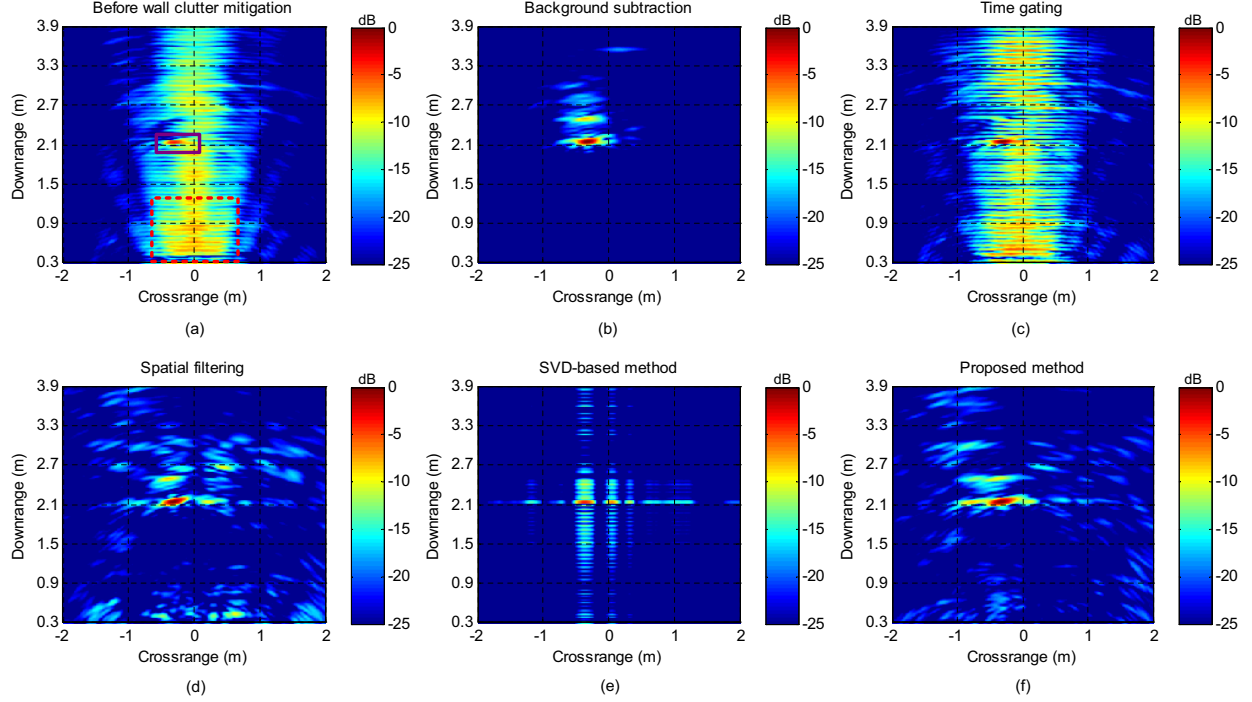


Fig. 15. Image of the first scene obtained using different wall clutter mitigation method: (a) no wall clutter mitigation, (b) background subtraction, (c) time gating, (d) spatial filtering, (e) SVD-based method and (f) proposed subspace projection method. The solid and dash rectangular regions in (a) represent the target and clutter areas for computing the TCR of the image.

With the availability of the background measurements, background subtraction produces a clear image as depicted in Fig. 15(b) in which most of the wall and background clutter is removed. With time gating, the formed image contains strong wall clutter, Fig. 15(c). Even though the target is far from the wall, time gating does not suppress the wall clutter because the wall reverberations and target reflections highly overlap in the time domain. The image in Fig. 15(d) shows spatial filtering is effective in removing the wall reflections without significantly compromising the target image. The existing SVD-based method in conjunction with AIC [16] produces an image where most of the wall clutter is suppressed but the shape of the target is distorted compared to that obtained from background subtraction, see Fig. 15(e). Figure 15(f) illustrates the image produced by the proposed subspace projection method, which is free of wall clutter and is as clear as that of the spatial filtering method. Figure 16 depicts the wall and target singular values identified by the proposed wall subspace estimation method. The singular values depicted in Fig. 16(a) belong to the wall and those shown in Fig. 16(b) belong to the target. From Fig. 16(a), we can see that the wall subspace consists of the first two dominant singular components and components 5, 23, 24 and 25. Furthermore, the non-dominant wall components are interleaved with the target components. Table III presents the improvement factor (IF) of the wall clutter mitigation methods for the images shown in Fig. 15. Background subtraction achieves the highest IF of 10.44 dB, followed by the proposed subspace projection method with an IF of 7.08 dB. Spatial filtering gives an IF of 3.72 dB. Among the SVD-based methods, the method based on a target

subspace spanned by the second singular vector achieves higher IF than those using AIC and MDL to determine the target subspace. Time gating achieves the worst performance with an IF of 1.45 dB.

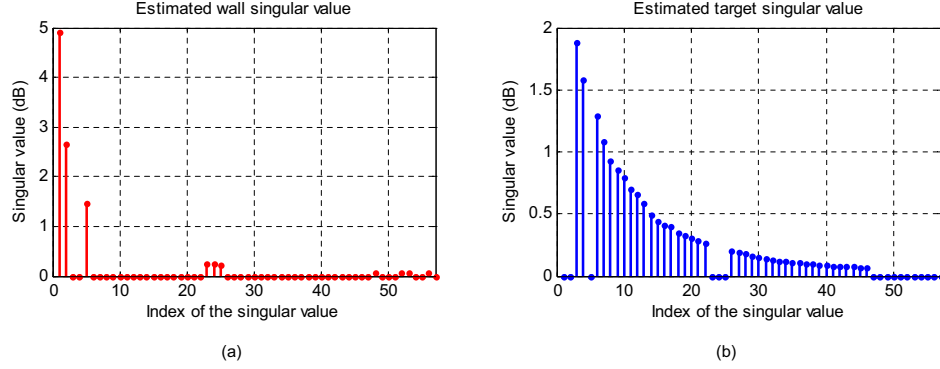


Fig. 16. Singular value spectrum of (a) the wall and (b) the target subspaces as identified by proposed wall subspace estimation method for scene with a dihedral behind the concrete wall.

TABLE III
IMPROVEMENT FACTOR OF THE WALL MITIGATION METHODS TESTED ON RADAR DATA COLLECTED FROM THE SCENE WITH THE DIHEDRAL BEHIND THE CONCRETE WALL.

Wall Clutter Mitigation method	Improvement factor (IF)
Proposed subspace projection method	7.08dB
Background subtraction	10.44dB
Time gating	1.45dB
Spatial filtering	3.72dB
SVD-based method [15] with target subspace spanned by second singular vector only	4.27dB
SVD-based method [16] with AIC	2.75dB
SVD-based method [16] with MDL	2.63dB

For the second scene comprising nine targets of different RCS behind a drywall, Fig. 17 depicts the formed images before and after wall clutter mitigation. Without any preprocessing, Fig. 17(a) depicts an image with strong wall clutter. With the availability of an empty scene, background subtraction produces a clear radar image, as shown in Fig. 17(b). Time gating and spatial filtering fail to remove the wall contributions from the radar data, see Figs. 17(c) and (d). The existing SVD-based methods also cannot suppress the wall clutter in the formed radar image. Figure 17(e) shows the output image from the SVD-based method with AIC; only the targets with large RCS are slightly visible. Figure 17(f) shows the image obtained using the proposed wall clutter mitigation method. In this image, the wall clutter is significantly reduced and the targets are as clear as those of background subtraction. Table IV displays the IF of the images presented in Fig. 17. The proposed method achieves the highest IF of 13.03 dB, followed by background subtraction with an IF of 12.73 dB. Surprisingly, spatial filtering and the SVD method as described in [15] give the lowest IFs of 5.47 dB and 5.37 dB, respectively. These results demonstrate that the

proposed method can be as effective as background subtraction in removing clutter due to both homogeneous and heterogeneous walls. In the next section, we apply the proposed method to wall clutter mitigation in 3-D TWRI.

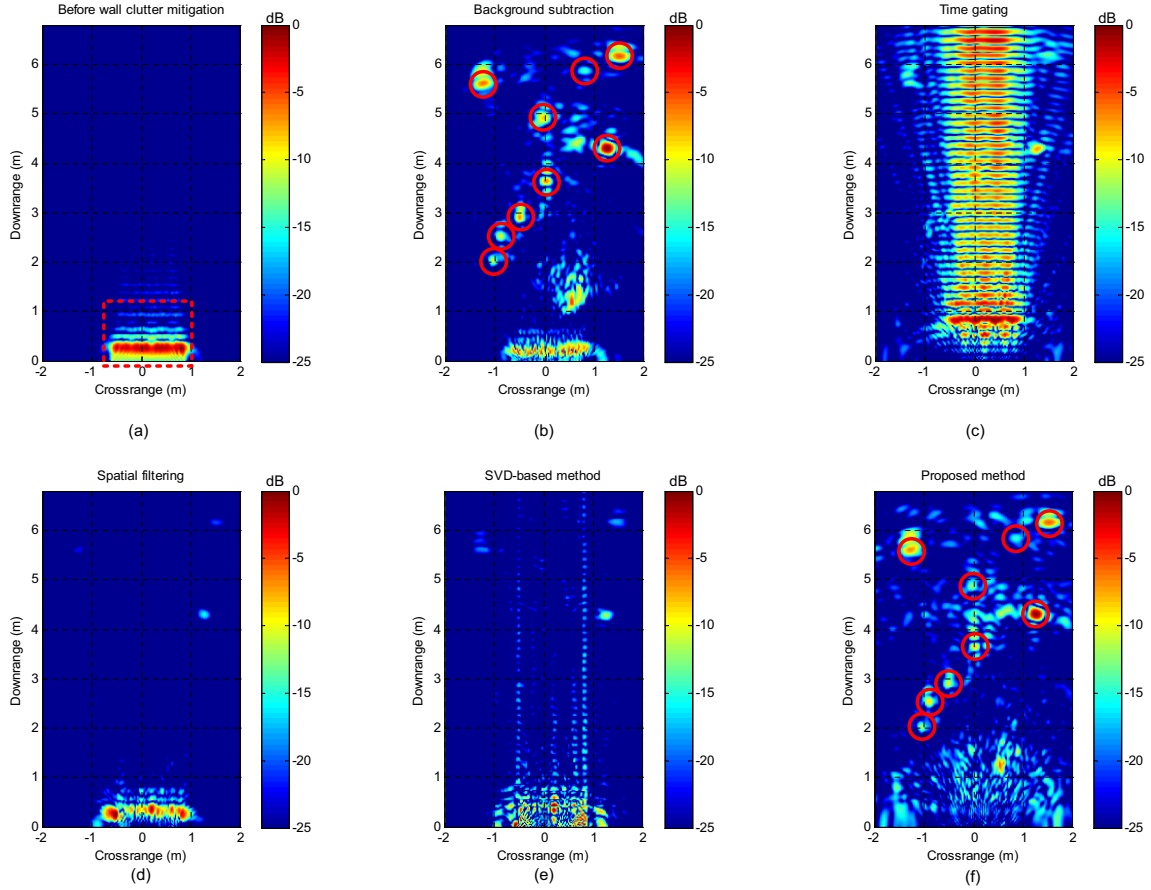


Fig. 17. Image of the populated scene obtained from the following wall clutter mitigation method: (a) no wall clutter mitigation, (b) background subtraction, (c) time gating, (d) spatial filtering, (e) SVD-method and (f) proposed subspace projection method. The solid rectangular region in (a) denote the clutter area for computing IF.

TABLE IV
IMPROVEMENT FACTOR OF WALL MITIGATION METHODS BASED ON THE SCENE WITH NINE TARGETS BEHIND THE DRYWALL.

Wall Clutter Mitigation Approach	Improvement factor (IF)
Proposed subspace projection method	13.03dB
Background subtraction	12.73dB
Time gating	7.99dB
Spatial filtering	5.47dB
SVD-based method [15] with target subspace spanned by second singular vector only	5.37dB
SVD-based method [16] with AIC	7.48dB
SVD-based method [16] with MDL	6.77dB

C. Three-Dimensional Through the Wall Radar Imaging

For 3D imaging, the scene is scanned by a 2-D array aperture along the horizontal and vertical directions to reveal the properties of targets residing behind the wall, e.g., the height of the target. The received monochromatic signals for all M frequencies at each antenna location of the 2-D array aperture are stacked to form a column of matrix B , $B \in \mathbb{C}^{M \times N}$, where N is the total number of antenna locations in the 2-D array aperture. The order of selecting the antenna locations, i.e., processing row-wise or column-wise, only results in a permutation of the columns of B . It can be readily shown that the permutation of the columns of the matrix B does not change the column order of the left and right singular vectors, and more importantly, it does not affect the singular values. Hence, the arrangement of the received signals into a matrix B does not affect the wall and target subspaces. To form 3-D images, DS beamforming is applied to compute the complex amplitude of each voxel $I(z, x, y)$:

$$I(z, x, y) = \frac{1}{NM} \sum_{n=0}^{N-1} \sum_{m=0}^{M-1} S(m, n) \exp(j\omega_m \tilde{\tau}_n(z, x, y)), \quad (47)$$

where $\tilde{\tau}_n(z, x, y)$ is the focusing delay from the n -th antenna of the 2-D array aperture to the voxel at location (z, x, y) . The computation of the two-way propagation delay from an antenna to a voxel is described in [7].

The first scene (a dihedral behind the concrete wall) and the second scene (nine targets behind the drywall) were interrogated using a 2-D array aperture. Background subtraction and the proposed subspace projection method were then used to mitigate the wall returns. We should point out that for the sake of clarity, the voxels below -20 dB were thresholded in the 3-D images. Figure 18 illustrates the 3-D radar images of the first scene. Applying DS beamforming directly to the frequency-space measurements produces a cluttered 3-D image, as shown in Fig. 18(a). Figure 18(b) shows the image obtained from background subtraction, which is free of wall clutter. The image produced by the proposed wall clutter mitigation method is shown in Fig. 18(c). This image is as clear as that produced by background subtraction. For the second scene, the formed images, using background subtraction and the proposed method, are shown in Fig. 19; both images are free of wall clutter. Table V presents the IF of the thresholded 3-D images depicted in Figs. 18 and 19. The proposed subspace projection method gives an IF of 21.33 dB for the first scene and 27.20 dB for the second, compared to background subtraction, which yields IF values of 20.82 dB and 27.01 dB, respectively.

TABLE V
IMPROVEMENT FACTOR OF THE WALL CLUTTER MITIGATION METHODS FOR 3-D IMAGING.

Approach	3-D scene with single target	3-D scene with multiple targets
Proposed subspace projection method	21.33dB	27.20dB
Background subtraction	20.83dB	27.01dB

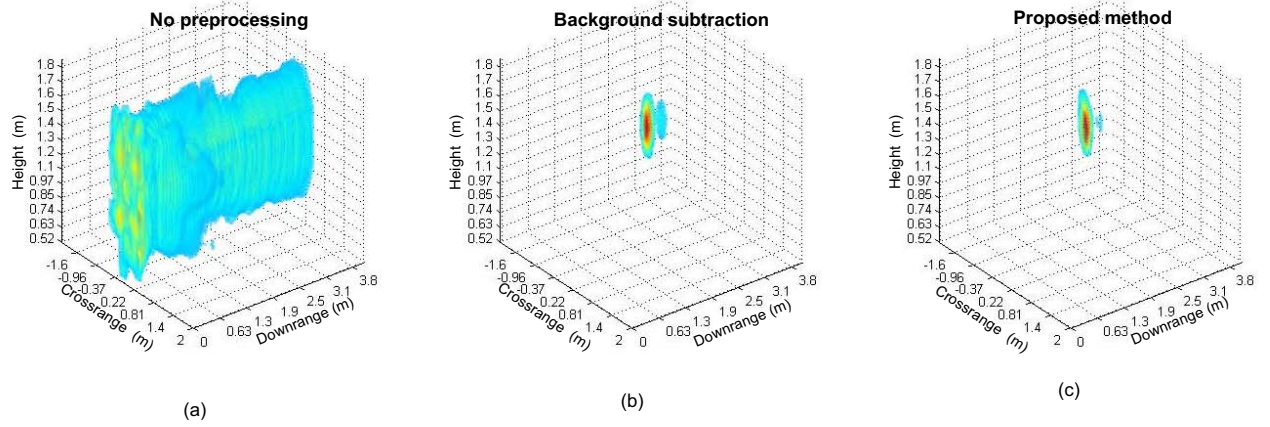


Fig. 18. The 3-D images of the first scene: (a) before wall clutter mitigation, after the use of (b) background subtraction, and (c) the proposed subspace projection method. For visualization, the 3-D images are displayed in linear scale and voxels less than -20 dB are removed.

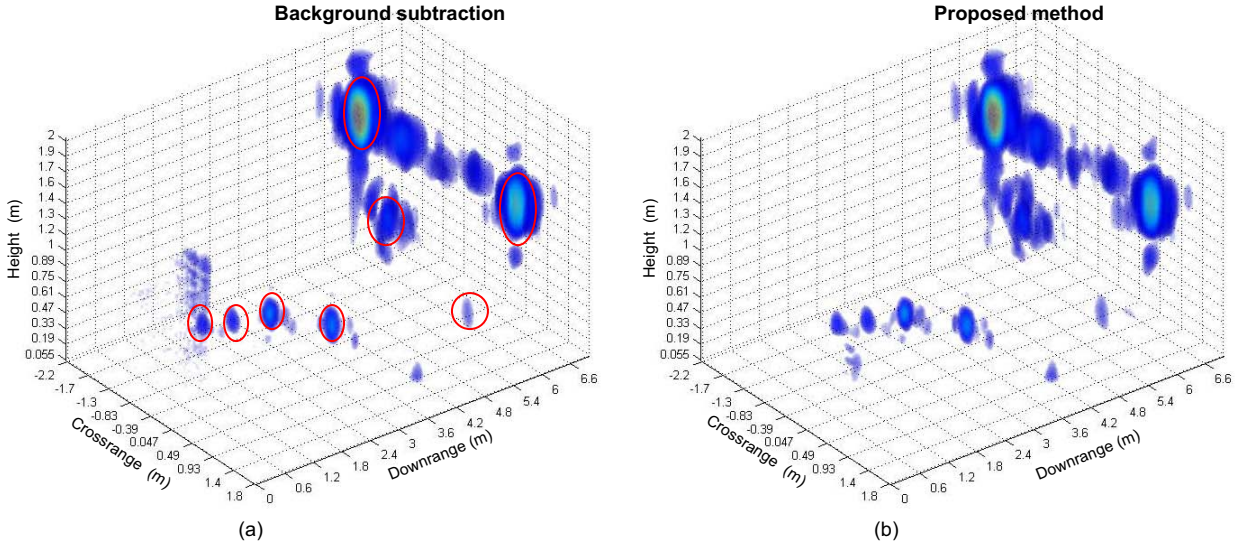


Fig. 19. The 3-D images of the second scene after the use of (a) background subtraction and (b) the proposed subspace projection method. For visualization, the 3D images are displayed in linear scale and voxels less than -20 dB are removed.

VI. CONCLUSION

Strong signal reflections from the front wall hinder the visibility of stationary targets in through-the-wall radar imaging. This paper provided an analysis of the eigen-structure of imaged TWRI scene. The analysis showed that when the radar is placed parallel to a homogeneous wall of uniform thickness, the wall returns span a one-dimensional subspace. However, when there are perturbations to the antenna alignment or non-uniformity of the wall thickness, which often occurs in practice, the wall subspace is no more one-dimensional but multi-dimensional.

For a heterogeneous wall, in which the dielectric properties vary in both dimensions, the wall returns span a multi-dimensional subspace. The analysis also showed that the target subspace is not limited to the second singular vector, as previously reported in the literature, but can be spanned by several singular vectors. Moreover, the dimension of the target subspace is determined by the location and the spatial extent of the target, the number of targets in the scene, and the configuration of the antenna array.

For wall clutter mitigation, we proposed a method that estimates the wall subspace and a subspace projection approach to remove, or at least significantly suppress, the wall clutter. The proposed approach does not assume prior knowledge of the scene and the wall electromagnetic characteristics. It was applied to demonstrate for wall clutter mitigation in real 2-D and 3-D TWRI data. Experiments with simulated and real data showed that the proposed method was as effective as background subtraction in removing wall clutter and revealing the behind-the-wall targets—without prior knowledge of the background scene.

APPENDIX A

OTSU THRESHOLDING METHOD

Suppose we have N singular values which lie in the range $[0, \sigma_{max}]$, and the spectrum of singular values is divided into L equal intervals $[\xi_i, \xi_{i+1})$, for $i = 0, \dots, L-1$. Let $P(\xi_i)$ denote the probability mass defined by the relative frequency of singular values in the i -th interval; that is,

$$P(\xi_i) = n(\xi_i)/N,$$

where $n(\xi_i)$ is the number of singular values $\sigma_i \in [\xi_i, \xi_{i+1})$. For a given threshold $\tau = \xi_k$, $k = 0, \dots, L-1$, the spectrum of singular values can be partitioned into two classes: $\mathcal{C}_w = \{\sigma_i \geq \tau\}$ and $\mathcal{C}_t = \{\sigma_i < \tau\}$. The class means of \mathcal{C}_w and \mathcal{C}_t are, respectively,

$$\mu_w(\tau) = \frac{1}{P_w(\tau)} \sum_{i=i_\tau}^{L-1} \xi_i P(\xi_i) \quad (48)$$

$$\mu_t(\tau) = \frac{1}{P_t(\tau)} \sum_{i=0}^{i_\tau-1} \xi_i P(\xi_i) \quad (49)$$

where i_τ denotes the index of the left endpoint of the interval that includes τ , and $P_w(\tau)$ and $P_t(\tau)$ are normalizing constants given by

$$P_w(\tau) = \sum_{i=i_\tau}^{L-1} P(\xi_i) \quad \text{and} \quad P_t(\tau) = \sum_{i=0}^{i_\tau-1} P(\xi_i).$$

The total mean of the classes, which is independent of τ , is

$$\mu_0(\tau) = \sum_{i=i_\tau}^{L-1} \xi_i P(\xi_i) \quad (50)$$

The optimum Otsu threshold is obtained by maximizing the between class variance

$$\tau^* = \arg \max_{\tau} \{\Sigma_0(\tau)\}, \quad (51)$$

where the between class variance is given by

$$\Sigma_0(\tau) = P_w(\tau)[\mu_w(\tau) - \mu_0]^2 + P_t[\mu_t(\tau) - \mu_0]^2.$$

APPENDIX B

REFLECTION AND TRANSMISSION COEFFICIENTS OF A LOSSY DIELECTRIC SLAB

For a lossy homogeneous wall of thickness d and complex dielectric permittivity $\epsilon = \epsilon' - j\epsilon''$, where ϵ' and ϵ'' are the real and imaginary parts of the dielectric permittivity, respectively, the propagation constant of the dielectric slab γ is defined in terms of the attenuation coefficient α and the phase factor β as

$$\gamma = \alpha + j\beta. \quad (52)$$

The attenuation coefficient α and the phase factor β are given by

$$\alpha = \omega_m \sqrt{\frac{\mu_0 \epsilon' \epsilon_0}{2}} \sqrt{\sqrt{1 + \left(\frac{\epsilon''}{\epsilon'}\right)^2} - 1} \quad (53)$$

and

$$\beta = \omega_m \sqrt{\frac{\mu_0 \epsilon' \epsilon_0}{2}} \sqrt{\sqrt{1 + \left(\frac{\epsilon''}{\epsilon'}\right)^2} + 1}, \quad (54)$$

where ω_m is the m -th angular frequency and μ_0 is the free space permeability. When an electromagnetic wave transmitted by the n -th antenna is incident at an angle θ_n relative to the normal of the interface between dissimilar media, the reflection $\Gamma_{v/h}$ and transmission $T_{v/h}$ coefficients are given by [24]

$$\Gamma_{v/h} = \frac{\rho_{v/h} \left(1 - \exp(-2\gamma \cos(\phi_n) d)\right)}{1 - \rho_{v/h}^2 \exp(-2\gamma \cos(\phi_n) d)} \quad (55)$$

and

$$T_{v/h} = \frac{(1 - \rho_{v/h}^2) \exp(-\gamma \cos(\phi_n) d)}{1 - \rho_{v/h}^2 \exp(-2\gamma \cos(\phi_n) d)}, \quad (56)$$

where $\rho_{v/h}$ is the Fresnel reflection coefficient, and the subscripts v and h denote, respectively, the vertical and horizontal polarizations; for a more detailed description of the Fresnel coefficient, the reader is referred to [25].

REFERENCES

- [1] M. G. Amin, (Ed.), *Through-the-wall radar imaging*, CRC Press, Boca Raton, FL, 2011.
- [2] M. Amin and K. Sarabandi, "Special issue on remote sensing of building interior," *IEEE Transactions on Geoscience and Remote Sensing*, vol. 47, no. 5, pp. 1267–1268, 2009.
- [3] M. Amin, "Special issue on advances in indoor radar imaging," *Journal of the Franklin Institute*, vol. 345, no. 6, pp. 556–722, 2008.
- [4] M. G. Amin and F. Ahmad, "Wideband synthetic aperture beamforming for through-the-wall imaging," *IEEE Signal Processing Magazine*, vol. 25, pp. 110–113, July 2008.
- [5] R. Dilsavor, W. Ailes, P. Rush, F. Ahmad, W. Keichel, G. Titi, and M. Amin, "Experiments on wideband through the wall imaging," in *Proc. of the SPIE Symposium on Defense and Security, Algorithms for Synthetic Aperture Radar Imagery XII Conference*, vol. 5808, 2005, pp. 196–209.
- [6] J. Moulton, S. A. Kassam, F. Ahmad, M. G. Amin, and K. Yemelyanov, "Target and change detection in synthetic aperture radar sensing of urban structures," in *Proc. of the IEEE Radar Conference*, 2008, pp. 1–6.

- [7] F. Ahmad, Y. Zhang, and M. G. Amin, "Three-dimensional wideband beamforming for imaging through a single wall," *IEEE Geoscience and Remote Sensing Letters*, vol. 5, no. 2, pp. 176–179, 2008.
- [8] Y.-S. Yoon and M. G. Amin, "Spatial filtering for wall-clutter mitigation in through-the-wall radar imaging," *IEEE Transactions on Geoscience and Remote Sensing*, vol. 47, no. 9, pp. 3192–3208, 2009.
- [9] M. Dehmollaian and K. Sarabandi, "Analytical, numerical, and experimental methods for through-the-wall radar imaging," in *Proc. of the IEEE International Conference on Acoustics, Speech and Signal Processing*, 2008, pp. 5181–5184.
- [10] M. Dehmollaian and K. Sarabandi, "Refocusing through building walls using synthetic aperture radar," *IEEE Transactions on GeoScience and Remote Sensing*, vol. 46, no. 6, pp. 1589–1599, 2008.
- [11] F. Abujarad, A. Jostingmeier, and A. S. Omar, "Clutter removal for landmine using different signal processing techniques," in *Proc. of the Tenth International Conference on Ground Penetrating Radar*, 2004, pp. 697–700.
- [12] F. Abujarad, G. Nadimy, and A. Omar, "Clutter reduction and detection of landmine objects in ground penetrating radar data using singular value decomposition (SVD)," in *Proc. of the Third International Workshop on Advanced Ground Penetrating Radar*, 2005, pp. 37–42.
- [13] A. N. Gaikwad, D. Singh, and M. J. Nigam, "Study of effect of room window on through wall imaging in UWB range," in *Proc. of the International Conference on Emerging Trends in Electronic and Photonic Devices and Systems*, 2009, pp. 395–398.
- [14] R. Chandra, A. N. Gaikwad, D. Singh, and M. J. Nigam, "An approach to remove the clutter and detect the target for ultra-wideband through-wall imaging," *Journal of Geophysics and Engineering*, vol. 5, no. 4, pp. 412–419, 2008.
- [15] P. K. Verma, A. N. Gaikwad, D. Singh, and M. J. Nigam, "Analysis of clutter reduction techniques for through wall imaging in UWB range," *Progress in Electromagnetics Research B*, vol. 17, pp. 29–48, 2009.
- [16] M. M. Riaz and A. Ghafoor, "Through-wall image enhancement based on singular value decomposition," *International Journal of Antennas and Propagation*, vol. 2012 (2012), Article ID 961829, 20 pages doi:10.1155/2012/961829
- [17] F. H. C. Tivive, M. G. Amin, and A. Bouzerdoum, "Wall clutter mitigation based on eigen-analysis in through-the-wall radar imaging," in *Proc. of the International Conference on Digital Signal Processing*, 2011, pp. 1–8.
- [18] F. H. C. Tivive, A. Bouzerdoum, and Moeness G. Amin, "An SVDbased approach for mitigating wall reflections in through-the-wall radar imaging," in *Proc. IEEE Radar Conference*, 2011, pp. 519–524.
- [19] Y.-S. Yoon and M. G. Amin, "High-resolution through-the-wall radar imaging using beamspace music," *IEEE Transactions on Antennas and Propagation*, vol. 56, no. 6, pp. 1763–1774, 2008.
- [20] C. A. Balanis, *Advanced Engineering Electromagnetics*, New York, NY: John Wiley and Sons, 1989.
- [21] R. Linnehan, J. Schindler, D. Brady, R. Kozma, R. Deming, and L. Perlovsky, "Dynamic logic applied to SAR data for parameter estimation behind walls," in *Proc. IEEE Radar Conference*, 2007, pp. 850–885.
- [22] P. Protiva, J. Mrkvica, and J. Macháč, "Time delay estimation of UWB radar signals backscattered from a wall," *Microwave and Optical Technology Letters*, Vol. 53, no. 6, pp. 1444–1450, 2011.
- [23] N. Otsu, "A threshold selection method for gray level histograms," *IEEE Transactions on Systems, Man, and Cybernetics*, vol. 9, no. 1, pp. 62–66, 1979.
- [24] Y. Pinhasi, A. Yaholom, and S. Petnev, "Propagation of ultra wide-band signals in lossy dispersive media," in *Proc. of the IEEE International Conference on Microwaves, Communications, Antennas and Electronic Systems*, 2008, pp. 1–10.
- [25] I. M. Besieris, "Comment on the corrected fresnel coefficients for lossy materials," *IEEE Antennas and Propagation Magazine*, vol. 53, no. 4, pp. 161–164, 2011.